Megalin, cubilin, and Dab2 drive endocytic flux in kidney proximal tubule cells

Youssef Rbaibi[a,†], Kimberly R. Long[a,†], Katherine E. Shipman[a], Qidong Ren[b], Catherine J. Baty[a], Ossama B. Kashlan[a], and Ora A. Weisz[a,*]

[a]Renal Electrolyte Division, Department of Medicine, University of Pittsburgh School of Medicine, Pittsburgh, PA 15213; [b]School of Medicine, Tsinghua University, Beijing, China, 100084

ABSTRACT **The kidney proximal tubule (PT) elaborates a uniquely high-capacity apical endocytic pathway to retrieve albumin and other proteins that escape the glomerular filtration barrier. Megalin and cubilin/amnionless (CUBAM) receptors engage Dab2 in these cells to mediate clathrin-dependent uptake of filtered ligands. Knockout of megalin or Dab2 profoundly inhibits apical endocytosis and is believed to atrophy the endocytic pathway. We generated CRISPR/Cas9 knockout (KO) clones lacking cubilin, megalin, or Dab2 expression in highly differentiated PT cells and determined the impact on albumin internalization and endocytic pathway function. KO of each component had different effects on the concentration dependence of albumin uptake as well its distribution within PT cells. Reduced uptake of a fluid phase marker was also observed, with megalin KO cells having the most dramatic decline. Surprisingly, protein levels and distribution of key endocytic proteins were preserved in KO PT cell lines and in megalin KO mice, despite the reduced endocytic activity. Our data highlight specific functions of megalin, cubilin, and Dab2 in apical endocytosis and demonstrate that these proteins drive endocytic flux without compromising the physical integrity of the apical endocytic pathway. Our studies suggest a novel model to explain how these components coordinate endocytic uptake in PT cells.**

Monitoring Editor
Robert Parton
University of Queensland

Received: Nov 14, 2022
Revised: Mar 27, 2023
Accepted: Apr 17, 2023

INTRODUCTION

Proximal tubule (PT) cells elaborate a unique and high-capacity apical endocytic pathway consisting of a dense array of vesicular and tubular structures that is required for the efficient recovery of albumin and other proteins that escape the glomerular filtration barrier. Two large receptors, megalin and CUBAM (consisting of three cubilin proteins bound to a single transmembrane chaperone amnionless [AMN; Larsen *et al.*, 2018]), are expressed abundantly in PT cells and mediate the binding and internalization of the broad array of filtered proteins that normally enter the tubule lumen (Christensen *et al.*, 2012; Eshbach and Weisz, 2017). The cytoplasmic tails of megalin and amnionless (AMN) contain NPXY and NPXF motifs, respectively, that engage the clathrin adaptor protein Dab2 to enable endocytic uptake of the receptors via clathrin coated pits that form at the base of PT microvilli (Oleinikov *et al.*, 2000; Pedersen *et al.*, 2010). After uncoating, endocytic vesicles fuse with apical early endosomes, where luminal acidification triggers ligand dissociation from their receptors. Ligands are retained within fluid-rich maturing endosomal compartments and ultimately delivered to lysosomes for degradation, while megalin and CUBAM are recycled to the apical membrane in tubular structures.

In addition to the need for a robust endocytic pathway for the retrieval of filtered proteins, endocytic trafficking also regulates the steady state distribution of PT ion and solute transporters essential for driving reabsorption along the nephron. Changes in glomerular filtration rate trigger rapid adjustments in ion transport needed to maintain tubuloglomerular balance (Duan *et al.*, 2010; Wang *et al.*, 2017). In some cases, these changes reflect alterations in the endocytosis or recycling of specific transporters. For example, acute increases in blood pressure result in rapid endocytosis of the apical Na^+–P_i cotransporter NaPi2 (Riquier *et al.*, 2009). In addition, changes in flow or the accompanying fluid shear stress have been

This article was published online ahead of print in MBoC in Press (http://www.molbiolcell.org/cgi/doi/10.1091/mbc.E22-11-0510 on April 26, 2023).

†These authors contributed equally to this work.

*Address correspondence to: Ora A. Weisz (weisz@pitt.edu).

Abbreviations used: AMN, amnionless; CHC, clathrin heavy chain; CUBAM, cubilin/amnionless; EEA1, early endosome antigen 1; KO, knockout; PT, proximal tubule.

shown to reversibly alter endocytic capacity (Raghavan *et al.*, 2014; Long *et al.*, 2017). How the balance of endocytosis and recycling is altered to accommodate the competing demands of reduced ion transporter uptake and increased endocytosis of filtered proteins under conditions of increased flow remains unclear.

Despite its essential role in PT function, we know surprisingly little about how the apical endocytic pathway is organized or regulated. It is clear, however, that loss of megalin expression has a profound effect on endocytic uptake. This effect extends beyond the internalization of megalin and CUBAM ligands, as evidenced by a striking loss of fluid phase uptake in the pronephros of zebrafish with mutations that compromise megalin expression (Kur *et al.*, 2011). Additionally, loss of megalin expression in zebrafish, in humans with Donnai–Barrow syndrome, and in mice has been suggested to reduce the density of PT clathrin-coated pits and subapical compartments (Leheste *et al.*, 1999; Kur *et al.*, 2011; Dachy *et al.*, 2015). These findings have led to the emerging dogma that expression of megalin in PT cells is needed to maintain the physical integrity of the apical endocytic pathway. A significant limitation of these ultrastructural studies is that the conclusions are based on examination of limited regions of only a few cells, and no morphometric comparison of KO vs. control tissues has been performed. Whether or how cubilin and/or Dab2 expression contributes to this process is also unclear. PTs of *Dab2* KO mice were reported to contain fewer clathrin coated pits and subapical endosomes than in controls, as well as to exhibit a possible reduction in megalin expression (Morris *et al.*, 2002b; Nagai *et al.*, 2005). And while changes in the endocytic pathway have not been reported in the PTs of Imerslund–Gräsbeck patients with cubilin mutations or in cubilin KO mice, reduced numbers of endocytic compartments were observed in visceral endoderm of *Cubn* KO mice and in *Drosophila* nephrocytes depleted of cubilin (Kozyraki *et al.*, 2001; Amsellem *et al.*, 2010; Zhang *et al.*, 2013; Perea-Gomez *et al.*, 2019).

Here we set out to examine the distinct roles that cubilin, megalin, and Dab2 play in maintaining apical endocytic uptake and the endocytic compartments themselves in PT cells. To this end, we used CRISPR/Cas9 technology to generate KO clones lacking expression of cubilin (*Cubn* KO), megalin (*Lrp2* KO), or Dab2 (*Dab2* KO) and examined the consequences on albumin uptake and on the integrity of the endocytic pathway. We performed our studies in the opossum kidney (OK) cell line cultured under continuous orbital shear stress, which we have found to improve their similarity to PT cells in vivo. In addition to an ~five-fold increase in apical endocytic capacity, and increased numbers of apical endocytic compartments, OK cells cultured under shear stress develop more apical microvilli and basolateral membrane infoldings, as seen in vivo (Long *et al.*, 2017). Moreover, these cells have more mitochondria, and utilize oxidative vs glycolytic metabolism compared with cells cultured under static conditions (Long *et al.*, 2017; Ren *et al.*, 2019). Under our culture conditions, megalin and cubilin are among the most highly expressed transcripts in OK cells, further underscoring the utility of these cells as a model in which to study the PT endocytic pathway (Park *et al.*, 2020). Using our CRISPR/Cas9 KO cells, we have identified distinct roles for each protein component in the endocytic uptake of albumin. Moreover, our studies suggest that while megalin, cubilin, and Dab2 contribute to overall PT endocytic flux, their expression is not needed to maintain the physical integrity of the endocytic pathway per se. Studies in *Lrp2* KO mice support our conclusions. Our work sheds new light on the roles of these proteins in PT function and suggests mechanisms that may explain their involvement in maintaining overall PT endocytic capacity.

RESULTS

Generation of CRISPR/Cas9 knockout clones

We used CRISPR/Cas9 technology to generate *Cubn* KO, *Lrp2* KO, and *Dab2* KO cell lines in OK cells (Long *et al.*, 2022). Control clones were isolated from cells transfected without guide sequences. The allelic mutations identified in these KO clones are shown in Figure 1A, and key results were validated in a duplicate set of KO clones with distinct allelic mutations (Supplemental Figure S1). Western blotting confirmed that each clone lacked detectable expression of the targeted protein (Figure 1B, Supplemental Figure S1). We observed a small but reproducible decrease in *Dab2* and *Lrp2* levels in the *Cubn* KO clone relative to control cells (Figure 1B). This trend was not apparent in the duplicate set of KO clones and may represent clonal variation (Supplemental Figure S1B).

Previous studies in megalin, cubilin, and Dab2 KO mice have documented an increase in urinary excretion of filtered proteins, suggesting a defect in PT endocytic uptake (Leheste *et al.*, 1999; Morris *et al.*, 2002b; Amsellem *et al.*, 2010). As predicted, CRISPR/Cas9 KO clones exhibited markedly reduced uptake of Alexa-Fluor-647 albumin (40 µg/ml) measured by spectrofluorimetry (Figure 1C, Supplemental Figure S1C). In contrast, the control clone exhibited uptake comparable to that of the parental OK cell line (Figure 1C).

Albumin uptake distribution differs between Cubn KO, Lrp2 KO, and Dab2 KO cells

To further assess the consequences of the differential effects of *Cubn* KO, *Lrp2* KO, and *Dab2* KO on the apical endocytic pathway, we exposed cells to 40 µg/ml apically added AlexaFluor-647 albumin for 15 min at 37°C, and then rapidly washed and fixed the cells. Confocal imaging of these samples revealed striking differences in the binding and uptake of albumin among KO clones (Figure 2). In control cells, albumin uptake was visible in numerous punctate compartments scattered throughout the subapical surface (Figure 2). Faint staining at the cell periphery was also observed in some cells. In contrast, uptake in *Cubn* KO cells was considerably reduced and albumin was present in smaller, more diffusely distributed punctae compared with controls (Figure 2). In *Lrp2* KO cells, a diffuse pattern of fluorescent albumin distributed across the apical plasma membrane was observed, along with a few punctae (Figure 2). Finally, in *Dab2* KO cells, we observed a striking accumulation of fluorescent albumin at the cell periphery, in addition to a few small punctate structures (Figure 2).

Contribution of cubilin, megalin, and Dab2 to saturable and nonsaturable albumin uptake components

The PT exhibits a remarkable capacity to recover high concentrations of albumin under nephrotic conditions. We previously used siRNA technology and mathematical deconvolution to assess the roles of cubilin, megalin, and Dab2 in concentration-dependent albumin uptake (Ren *et al.*, 2020). Our studies suggested that apical albumin uptake in OK cells is mediated by two saturable binding components with high (C1, ~50 µg/ml) and low (C2, ~300 µg/ml) affinities, along with a nonsaturable uptake component (C3) that likely represents fluid phase uptake (Ren *et al.*, 2020).

We performed similar albumin uptake curves and deconvolution analysis using our CRISPR/Cas9 KO clones. As shown in Figure 3A, albumin uptake along a wide range of concentrations ranging from normally filtered to nephrotic levels was markedly reduced in *Cubn* KO, *Lrp2* KO, and *Dab2* KO cell lines compared with that of control cells. Deconvolution of the fitted uptake curves into individual components revealed the contribution of each component to overall

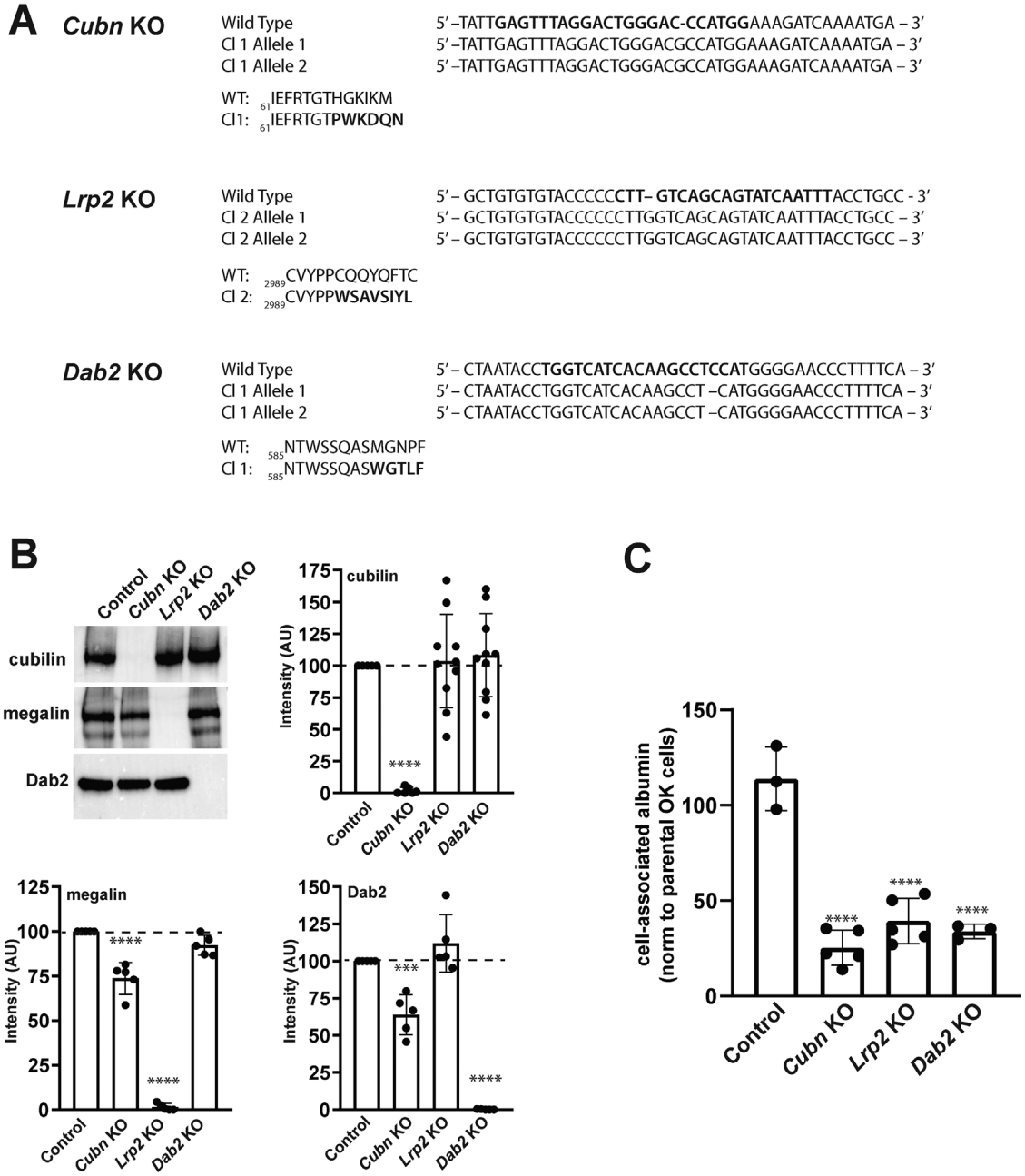

FIGURE 1: CRISPR/Cas9 knockout of *Lrp2*, *Cubn*, or *Dab2* impairs OK cell endocytic uptake of albumin. (A) Allelic indel sequences for CRISPR/Cas9 *Cubn* KO, *Lrp2* KO, and *Dab2* KO clones relative to Control nucleotide and amino acid sequences are shown. (B) Equivalent amounts (15 µg) of cell lysates from control, *Cubn* KO, *Lrp2* KO, and *Dab2* KO clones were Western blotted with antibodies against cubilin, megalin, and Dab2. Representative blots are shown, along with quantitation of blots from at least three independent experiments with values normalized to intensities in control cells. ****$p < 0.0001$, ***$p < 0.001$, by one-way ANOVA relative to control. (C) Parental OK cells and control and KO clones were incubated for 30 min with apically added AlexaFluor-647 albumin and washed, and cell-associated fluorescence was quantified by spectrofluorimetry. Data from three to five independent experiments (mean ± SD, normalized to parental OK cells) are plotted. ****$p \leq 0.0001$ by one-way ANOVA.

uptake at a given concentration of albumin, and is most easily visualized in semilog plots (Figure 3, B–E). Similarly to our previous observations using siRNA, there was a preferential reduction in the high-affinity uptake component (C1; red lines; 20 µg/mL) in *Cubn* KO cells and in the low-affinity uptake component (C2; green lines; 200 µg/mL) in *Lrp2* KO cells. KO of *Dab2* impacted both uptake components. Strikingly, uptake via the nonsaturable component (C3; blue lines) was also reduced in all of the KO cell lines. Figure 3, F–H shows a direct comparison of the capacity (*V*) of each component in the CRISPR/Cas9 KO clones. Knockout of *Cubn* nearly abolished the capacity of the high-affinity component V1 (Figure 3F), whereas the V2 (green) component was absent in *Lrp2* KO clones (Figure 3G). As a consequence, the V2/V1 ratio was increased in *Cubn* KO cells, decreased in *Lrp2* KO cells, and essentially unchanged in *Dab2* KO cells (Figure 3I). The capacity of the nonsaturable site (extrapolated to linear uptake at 20 mg/ml) was

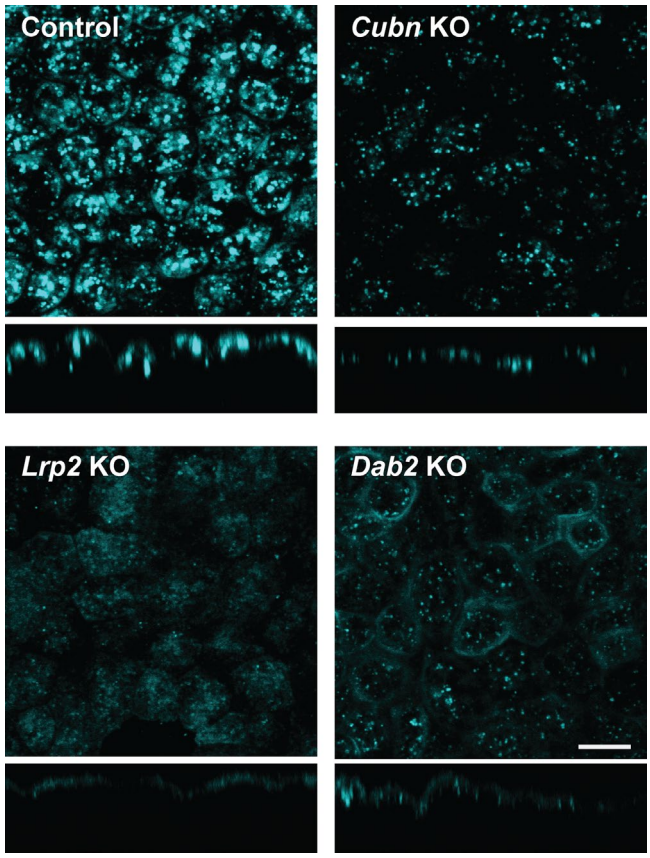

FIGURE 2: CRISPR/Cas9 KO cell lines exhibit different patterns of albumin binding and uptake. Control, *Cubn* KO, *Lrp2* KO, and *Dab2* KO cells were incubated with 50 µg/ml AlexaFluor-647 albumin for 15 min at 37°C and then fixed and visualized by confocal microscopy. Representative *xz* sections are shown below each panel. Scale bar: 10 µm.

significantly reduced in all KO clones compared with controls, with *Lrp2* KO having the greatest effect (Figure 3H). This is consistent with our previous observations quantifying dextran uptake in siRNA knockdown cells (Ren *et al.*, 2020). Together, our data suggest selective and independent functions of cubilin, megalin, and Dab2 in mediating the endocytic uptake of filtered proteins. Moreover, because KO of all proteins also impaired uptake of fluid phase markers, we considered whether the physical integrity of the apical endocytic pathway is compromised by loss of any of these proteins.

Expression of apical endocytic proteins is unaffected in CRISPR/Cas9 KO cells

The reduced endocytic capacity in our KO clones led us to examine the expression level and distribution of known markers of apical endocytic compartments, using antibodies that recognize OK cell proteins. Western blotting with antibodies against clathrin heavy chain (CHC), the Rab5 effector protein early endosome antigen 1 (EEA1), and the recycling endosome marker Rab11a revealed no quantitative changes in expression of these proteins compared with control cells (Figure 4, A–C; Supplemental Figure S1). This is consistent with the absence of transcriptional changes in mRNA encoding these proteins in our KO clones (Long *et al.*, 2022). By confocal microscopy, we observed no qualitative differences in the distributions of CHC, Rab5, Rab7 (Supplemental Figure S2), EEA1, or Rab11a in control vs. KO cells (see Figure 6C). In some experiments, we did note apparent differences in the intensity of staining of a given marker in some KO clones; however, these observations were not reproducible between experiments, and likely reflect technical challenges in comparing signal intensities due to variations in cell heights between individual cells on permeable supports.

To confirm our observations, we performed ultrastructural imaging on control and KO cell lines (Figure 5). Similarly to our prior analysis of parental OK cells cultured under orbital shear stress (Long *et al.*, 2017), many regions of the subapical cytoplasm of control cells contained structures that resembled the apical endosomes, apical vacuoles, and dense apical tubules reported in PTs in vivo. We could readily find similar regions in *Cubn* KO, *Lrp2* KO, and *Dab2* KO cells (Figure 5). Together, these data suggest that loss of any of these proteins does not comprehensively impair the physical integrity of the apical endocytic pathway in OK cells.

Knockout of cubilin, megalin, or Dab2 reduces apical endocytic pathway flux in proximal tubule cells

To quantify the formation of apical endocytic compartment in our cells, we used fluorescently conjugated fixable dextran. There is no evidence for a clathrin-independent apical uptake pathway in PT cells, and control studies confirmed that fluorescently conjugated dextran and albumin largely colocalize in subapical endocytic structures when added to the apical medium of control cells for 3 min (Supplemental Figure S3). To visualize the earliest population of apical endosomes that receive internalized cargo, we incubated cells with fixable AlexaFluor 568-dextran for 3 min and then rapidly washed and fixed the cells. Dextran-positive compartments were quantified in randomly selected fields as described in *Materials and Methods* (Figure 6A). We used a longer incubation (60 min) to label compartments receiving fluid-phase cargo along the entire endosomal pathway, including lysosomes and recycling compartments (Figure 6B). In both cases, we observed a significant reduction in fluorescent endocytic compartments in the KO clones relative to control cells ($p < 0.0001$). KO of megalin had the most profound effect, resulting in nearly the complete absence of fluorescent compartments. These data suggest that the formation and maturation of endocytic vesicles is profoundly affected by KO of megalin and Dab2, and moderately by loss of cubilin.

To examine this in greater detail, we incubated cells for 3 min with fixable AlexaFluor 568-dextran and then fixed and processed cells to detect EEA1 or Rab11a (Figure 6C). The distribution and intensity of Rab11a staining was indistinguishable between control, *Cubn* KO, *Lrp2* KO, and *Dab2* KO clones. Although EEA1-positive punctae appeared dimmer in *Lrp2* KO cells than in the other cell lines in the experiment shown, differences in apparent marker intensities between cell lines likely reflect variations in the proximity of the filter to the image plane and were not reproducibly observed. Indeed, quantitation of the number and area of EEA1-positive compartments revealed no differences between control and KO clones (Supplemental Figure S4). Internalized dextran in control clones was readily observed in compartments and clusters of varying sizes, most of which were also positive for EEA1. This pattern is consistent with the observation that ferritin reaches apical vacuoles within 5 min of uptake in rat PT (Maunsbach, 1966) and with the very rapid maturation of apical endocytic compartments predicted by our recent mathematical model of membrane traffic in OK cells (Shipman *et al.*, 2022). In contrast, there was a dramatic reduction in dextran uptake in KO clones, consistent with our quantitative data in Figure 6A and B. Dextran-positive compartments in *Cubn* KO cells were similar in appearance to those in control cells, albeit less numerous. In contrast, the small amount of dextran internalized in *Lrp2* KO and

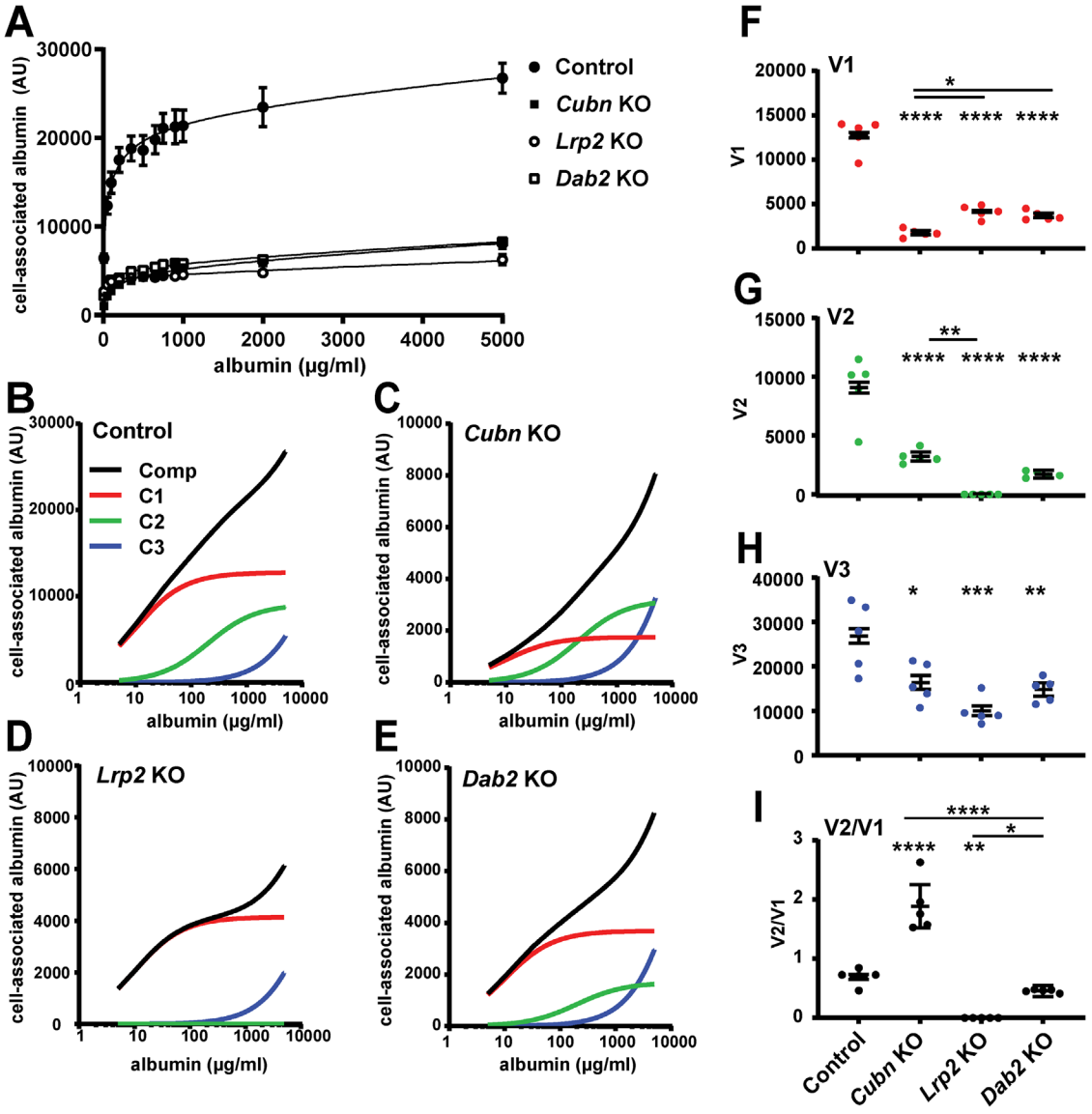

FIGURE 3: CRISPR/Cas9 KO of cubilin, megalin, or Dab2 differentially affects concentration-dependent albumin uptake profiles. (A) CRISPR/Cas9 control, *Cubn* KO, *Lrp2* KO, and *Dab2* KO clones were incubated with the indicated concentrations of Alexa Fluor-647 albumin for 15 min and then washed, and cell-associated fluorescence was quantified. The mean ± SD of five experiments is plotted, together with the fitted curves for each condition. (B–E) Data from the experiments above were deconvolved and the composite line (Comp, black) and high-affinity (C1, red), low-affinity (C2, green), and nonsaturable (C3, blue) albumin uptake components were plotted on a semilog scale to better visualize the differential effects of *Cubn* KO on high-affinity albumin uptake (C1) and *Lrp2* KO on low-affinity uptake (C2). The capacities of (F) high-affinity (V1), (G) low-affinity (V2,) and (H) nonsaturable (V3, extrapolated to uptake at 20 mg/ml albumin) pathways in each cell line are plotted. (I) The ratio of V2/V1 components is plotted to highlight the changes in albumin affinity profile between the different KO cell lines. The uncertainty of the mean was propagated from the uncertainties of the fitted parameters in each experiment. Asterisks above each condition denote significance vs control; asterisks above the horizontal lines denote significance between other pairs. *$p < 0.05$; **$p < 0.01$; ***$p < 0.001$; ****$p < 0.0001$ by one-way ANOVA with multiple comparisons.

Dab2 KO cells remained confined to small punctae that presumably represent endocytic vesicles. We conclude that loss of cubilin, and more profoundly of megalin and Dab2, impairs flux through the apical endocytic pathway but does not dismantle the pathway itself.

At steady state, the majority of megalin in OK cells (>90%) is present in subapical compartments and colocalizes primarily with Rab11a (Shipman *et al.*, 2022). We therefore examined whether KO of cubilin, megalin, or Dab2 impacts the distribution of membrane receptors. To this end, we expressed a truncated megalin construct (minimegalin) containing an amino-terminal HA epitope and tagged at the carboxy terminus with mCherry. Albumin uptake was not restored in KO cells expressing this construct (unpublished data), suggesting that low levels of minimegalin are insufficient to rescue endocytic flux or that this construct does not recapitulate the structure or function of full-length megalin (Beenken *et al.*, 2023). Cells were processed to detect surface minimegalin using anti-HA antibody, and then fixed and stained to detect Rab11a. As shown in Figure 7, surface minimegalin, revealed by anti-HA antibodies, was localized

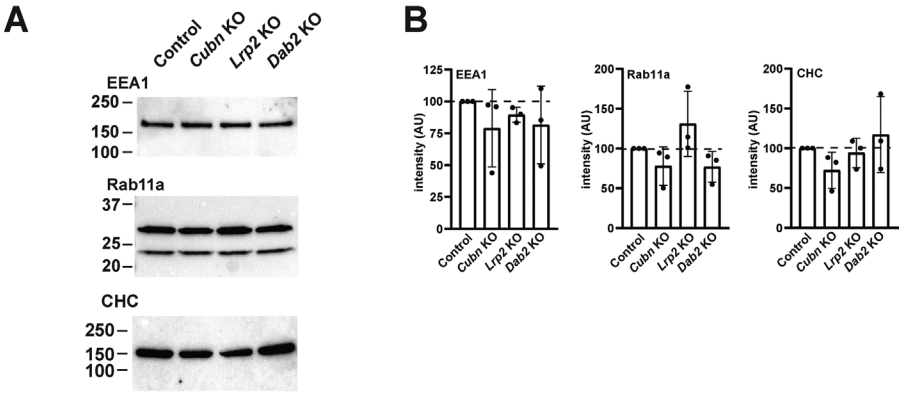

FIGURE 4: Expression of endocytic pathway proteins in CRISPR/Cas9 KO clones. (A) Equivalent amounts (15 µg) of cell lysates from CRISPR/Cas9 control, *Cubn* KO, *Lrp2* KO, and *Dab2* KO clones were Western blotted with antibodies against CHC, EEA1, and Rab11a. Representative blots are shown, with the migration of molecular mass markers (in kDa) indicated on the left. The upper band in the Rab11a doublet corresponds to the predicted molecular mass. (B) Quantitation of blots from three independent experiments with values normalized to that of control cells is shown. There was no significant difference in protein expression between the four cell lines by two-way ANOVA.

primarily to clusters on the apical membrane of control cells with a pattern strongly reminiscent of microvilli. In contrast, total megalin (mCherry staining) was distributed primarily to subapical compartments which overlapped considerably with Rab11a. This distribution of minimegalin is qualitatively similar to that of endogenous megalin in OK cells (Shipman *et al.*, 2022). The distribution of minimegalin in *Cubn* KO, *Lrp2* KO, and *Dab2* KO cells was indistinguishable from that in control cells (Figure 7). As a complementary approach, we quantified the surface expression of cubilin in OK cells and in control and CRISPR/Cas9 KO clones by cell surface biotinylation. As shown in When one author plus et al. is given, give the names of the first 10 authors plus et al. if more than Supplemental Figure S5, knockout of megalin or Dab2 had no effect on the surface/intracellular distribution of cubilin. Together, these data suggest that the loss of endocytic flux in these cells does not appreciably perturb the steady state partitioning of membrane proteins (Figure 7).

Structural integrity of the apical endocytic pathway is preserved in Lrp2-KO mice

Previous ultrastructural experiments have qualitatively observed profound decreases in coated pits, coated vesicles, and endocytic compartments in *Lrp2*-KO mice. Because these studies are necessarily limited to examination of a small number of cells whose subsegment identity along the PT axis cannot readily be confirmed, we used confocal imaging to examine whether the expression and distribution of apical endocytic compartments is altered in *Lrp2*-KO and wild-type mice. We previously showed that kidneys of EMX-*Lrp2* KO mice have >95% reduction in megalin expression (Long *et al.*, 2022). Cortical kidney sections from sex- and age-matched mice were costained to reveal megalin and cubilin, clathrin, Rab5, Rab7, Rab11a, or LAMP1. Strikingly, we observed no differences in the staining patterns or intensities of any of these markers in the occasional megalin-positive cell from with neighboring knockout cells in the same tubules (Figure 8). Ultrastructure analysis confirmed that PT cells in *Lrp2* KO mice elaborated a dense array of subapical compartments that were qualitatively indistinguishable from those in wild-type PTs, although we could not discern using this approach whether specific endocytic compartments were underrepresented (Supplemental Figure S6). Taken together, our data suggest that robust expression of megalin is needed to drive endocytic flux, but not to assemble or maintain the apical endocytic pathway in PT cells.

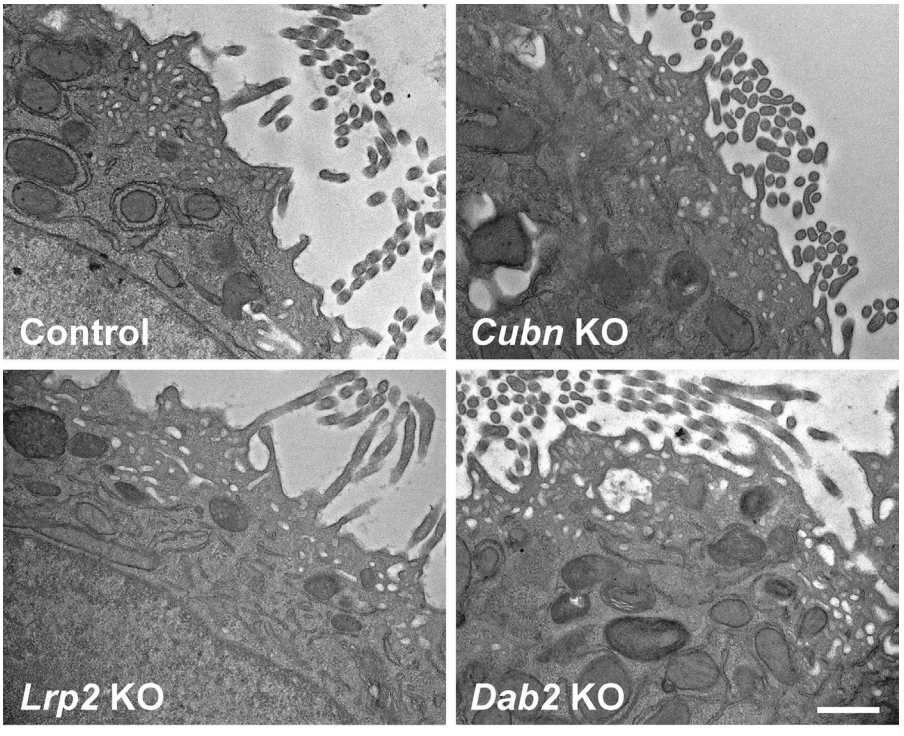

FIGURE 5: Electron microscopy of CRISPR/Cas9 knockout clones. CRISPR/Cas9 control, *Cubn* KO, *Lrp2* KO, and *Dab2* KO clones cultured under orbital shear stress on permeable supports were fixed and processed for electron microscopy as described in *Materials and Methods*. Representative images are shown. Scale bar: 500 nm.

DISCUSSION

The unique factors that enable the elaboration and maintenance of the remarkable apical endocytic apparatus of PT cells are poorly understood. Here we have used CRISPR/Cas9 technology to dissect the role of individual components of the machinery required for efficient uptake of filtered proteins by highly differentiated PT cells. We knocked out the multiligand receptors megalin and cubilin as well as their adaptor protein Dab2 and examined the consequences for the apical endocytic pathway and for the uptake of albumin, a normally filtered protein that is efficiently cleared from the tubule lumen by

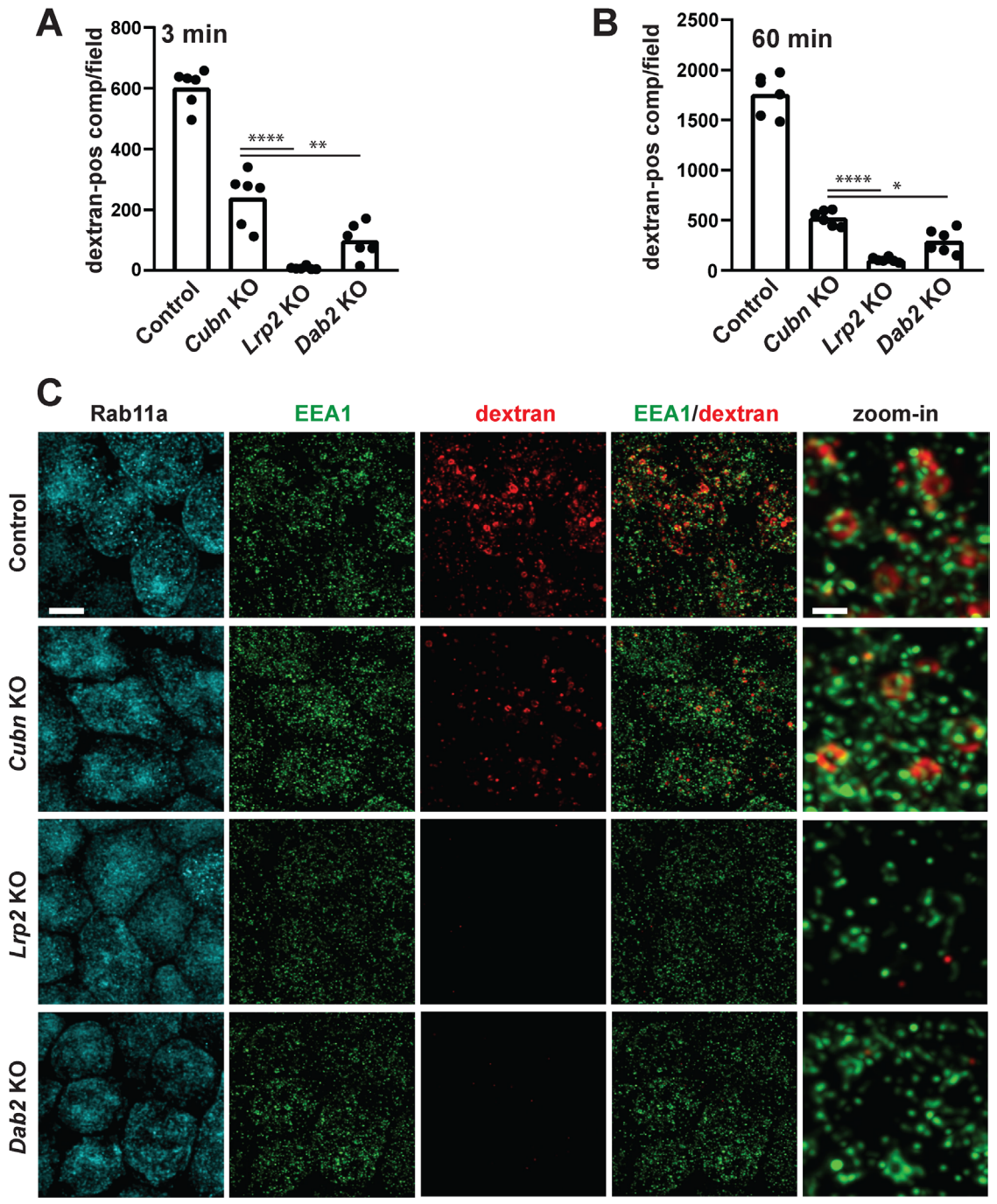

FIGURE 6: Reduced apical endocytic flux in CRISPR/Cas9 KO cells. CRISPR/Cas9 control, *Cubn* KO, *Lrp2* KO, and *Dab2* KO clones were incubated with apically added AlexaFluor-568 dextran for 3 min (A) or 60 min (B) and then fixed and imaged by confocal microscopy. Six randomly acquired fields of each sample were quantified as described in *Materials and Methods* to determine the number of early or total dextran-positive compartments. All samples were significantly different from controls by one-way ANOVA with Tukey's multiple comparisons test ($p < 0.0001$). Other comparisons that were statistically significant using this analysis are noted by the horizontal bars (*$p < 0.05$, **$p < 0.01$, ****$p < 0.0001$). (C) CRISPR/Cas9 control, *Cubn* KO, *Lrp2* KO, and *Dab2* KO clones were incubated with apically added AlexaFluor-568 dextran for 3 min and then fixed and processed to detect EEA1 and Rab11a. Representative confocal images for each fluorophore are shown, as well as merged and zoomed-in images of EEA1/dextran merged images. Note the rapid association of dextran-positive compartments with EEA1 and the formation of larger clusters as these endocytic compartments mature into larger vacuoles. Scale bar: 5 μm; 1 μm for zoom-ins.

the PT. Morphological and quantitative analysis of these cell lines shows that all three components are needed to maintain a maximally efficient apical endocytic pathway in OK cells. Of note, KO of any of these components appears to impair endocytic flux as monitored by uptake of the fluid phase marker dextran. Despite this, the physical integrity of the endocytic pathway was essentially intact. Similarly to our results in OK cells, clathrin, Rab5, Rab11a, and Lamp1 remain normally distributed in the PTs of *Lrp2* KO

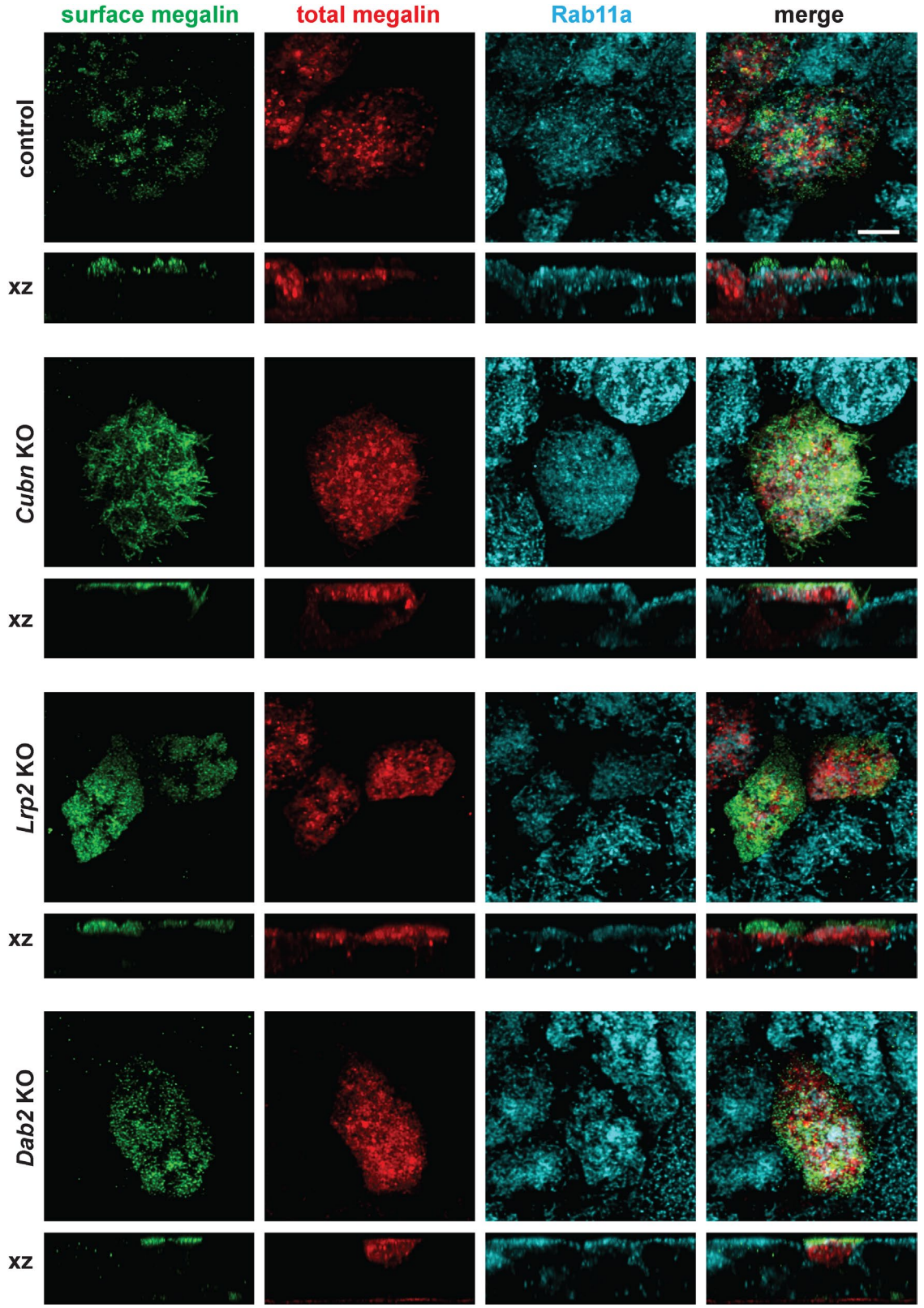

FIGURE 7: A mini-megalin construct is primarily localized to subapical compartments in control and CRISPR/Cas9 *Cubn* KO, *Lrp2* KO, and *Dab2* KO cells. Cells were transfected with a construct encoding HA-minimegalin-mCherry. Cells were fixed and incubated on ice with anti-HA antibody to label cell surface megalin, then permeabilized and processed to detect Rab11a. Surface (anti-HA) and total (mCherry) megalin distributions in each cell line are shown. Note the discordance in surface vs. total staining patterns in all cells ,consistent with the preferential localization of megalin to intracellular compartments. Scale bar: 5 μm.

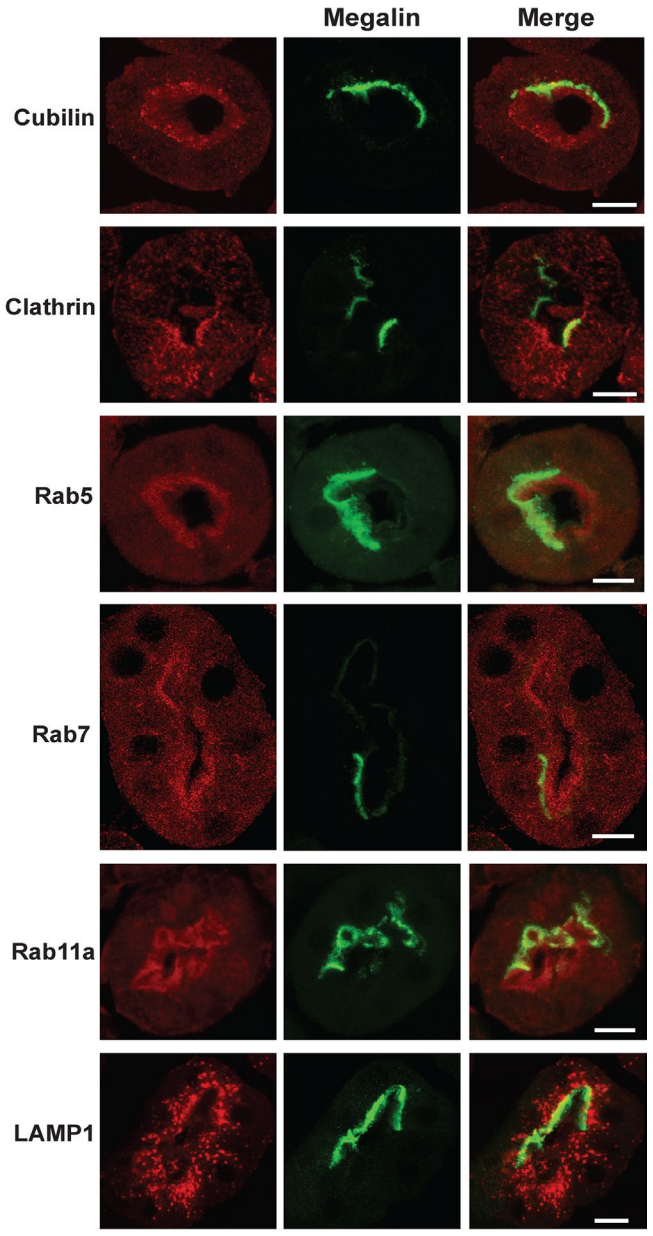

FIGURE 8: Apical endocytic pathway integrity in maintained in *Lrp2* KO mice. EMX-*Lrp2* KO mice were stained to detect megalin (green) and either cubilin, clathrin, Rab5, Rab11a, or LAMP1 (red). Individual and merged panels of tubules containing megalin-expressing and -nonexpressing cells are shown. Scale bars: 10 μm. Note the similar staining of all markers in megalin-expressing vs. -nonexpressing cells.

mice. While we cannot rule out subtle differences between control and KO clones, the presence of apparently normal Rab5, Rab11a, and Lamp1 staining in megalin-deficient cells is in contrast to previous reports tying impaired uptake to a dearth of subapical endocytic compartments in these cells. The involvement of CUBAM receptors in maintaining PT endocytic flux also has not been appreciated previously. Taken together, our data shift the paradigm of how the expression of megalin mediates endocytic function in the PT. Rather than being necessary to maintain compartments themselves, megalin (as well as Dab2, and to a lesser extent, CUBAM) expression governs the dynamics of transport between compartments.

Using our KO cell lines, we confirmed the distinct contributions of cubilin, megalin, and Dab2 to concentration-dependent albumin uptake (Ren *et al.*, 2020). Knockout of cubilin preferentially reduced the capacity for high-affinity uptake of albumin. Knockout of megalin reduced albumin uptake via this site as well (presumably by disrupting cubilin traffic; see below) and abolished lower-affinity uptake of albumin. Consistent with the role for Dab2 in clathrin-mediated uptake of megalin and CUBAM, uptake via both high- and low-affinity sites was coordinately inhibited in *Dab2* KO cells. While we drew similar conclusions from our previous study, the results we obtained here using CRISPR/Cas9 KO clones showed considerably less variance than those obtained using siRNA and provide additional confidence in our conclusions.

Remarkably, despite the large reduction in albumin and dextran uptake in KO cell lines compared with control cells, the expression levels of key endocytic components (CHC, EEA1, and Rab11a) was unchanged. This is consistent with RNASeq analysis confirming similar transcript levels for these proteins in KO and control cells (Long *et al.*, 2022). Moreover, the distributions of these proteins as visualized by confocal imaging and the ultrastructure of apical endocytic pathway components examined by electron microscopy were indistinguishable between the control cell line and KO cells, as well as in control and *Lrp2* KO mice. That said, there is considerable variability in the density of subapical compartments between EM sections in the same sample. This may have contributed to the previous conclusion that *Lrp2* KO mice have reduced levels of endocytic compartments.

One striking difference between KO cell lines was the distribution of cell-associated albumin after brief incubation with a physiological concentration of AlexaFluor-647 conjugated albumin. Albumin was present in endocytic compartments in *Cubn* KO cells, albeit in fewer and dimmer punctae than in control cells. We interpret this profile to reflect reduced internalization of low amounts of albumin captured by low affinity to megalin receptors in these cells. In contrast, albumin staining in *Lrp2* KO cells was diffuse and largely confined to the apical surface, with a minimal intracellular pool. The few apparent punctae in these cells may reflect high-affinity binding to CUBAM receptors "stranded" at the plasma membrane in the absence of megalin. In *Dab2* KO cells, we observed a few fluorescent punctae and a clear clustering of cell-associated albumin at the cell periphery.

Based on our aggregate data, we propose a new model to explain the individual roles of these three components in the uptake of filtered albumin by PT cells. In our model, cubilin is the primary binding receptor for normally filtered concentrations of albumin, whereas megalin plays an ancillary role in this process. Our data also show for the first time that cubilin expression contributes to maintaining apical endocytic flux in PT cells, as both quantitative and qualitative analyses revealed reduced dextran uptake in *Cubn* KO cells compared with control cells. Expression of key proteins in the endocytic pathway was unchanged and cannot account for our observations. This peripheral membrane pattern of Dab2 staining is reminiscent of the exocytic "hotspots" at the lateral edges of polarized kidney cells observed by Louvard when following the distribution of newly recycled aminopeptidase in MDCK cells (Louvard, 1980). We hypothesize that Dab2 may engage newly exocytosed receptors at these sites and ferry them to CCPs. Dab2 binding to the motor protein myosin VI has been suggested to facilitate its ability to cluster receptors into CCPs (Buss *et al.*, 2001; Morris *et al.*, 2002a; Maurer and Cooper, 2006). We attempted to knock down myosin VI to see whether this phenocopied the profile of albumin in *Dab2* KO cells but were unable to achieve sufficient depletion of the protein using multiple siRNA oligonucleotides.

Although megalin does not bind appreciably to normally filtered concentrations of albumin, it plays an outsized role compared with CUBAM in maintaining apical endocytic flux in PT cells, as evidenced by the greater reduction in fluorescent dextran uptake in *Lrp2* KO vs *Cubn* KO cells. Megalin expression was estimated to be ~sevenfold greater than that of AMN in the earliest (S1) segment of the rat PT in a recent quantitative proteomic study (Limbutara *et al*., 2020), and may thus more avidly engage the endocytic machinery to drive endocytic flux. A related possibility is that CUBAM receptors may engage Dab2 with lower affinity than megalin. Unlike megalin, which binds to Dab2 using canonical NPXY motifs, the cytoplasmic tail of AMN contains two NPXF sequences (Pedersen *et al*., 2010). While NPXF and NPXY sequences appear comparably able to engage Dab2 in cultured cells, the high evolutionary conservation of the NPXF motifs in AMN suggests some in vivo differences in function. Finally, megalin expression might also be needed to mediate signal transduction pathways needed to maintain endocytic pathway function. The cytoplasmic tail of megalin binds to numerous proteins and is subject to regulation by phosphorylation (Yuseff *et al*., 2007; De *et al*., 2014). Of note, the megalin tail contains a highly conserved SH2 binding domain that is predicted to engage the p85 regulatory subunit of class I PI3 kinase (Mellor *et al*., 2012). Impaired activation of this enzyme may contribute to reduced endocytic flux. Complementary -omics, morphological, and biochemical studies using the cell lines described here will facilitate further unraveling of the specific roles of cubilin, megalin, and Dab2 in the maintenance of PT endocytic function and ultimately guide strategies for treatment of PT injury.

MATERIALS AND METHODS

Generation and characterization of CRISPR/Cas9 KO clones

CRISPR/Cas9 KO clones in OK cells were generated and cultured as described in detail in Long *et al*. (2022) using the protocol in Invitrogen's TrueGuide Synthetic Guide RNA User Guide (Publication MAN0017058) with minor modifications. Briefly, guide sequences were subcloned into the pHRS surrogate reporter vector as described to enable subsequent selection of gene-edited clones (Pereira *et al*., 2016; Eshbach *et al*., 2017). OK cells (1×10^6 cells) were electroporated with RNP complexes and pHRS. Cells were treated for 48 h with hygromycin B starting 36–48 h postelectroporation, and clones were isolated by single-cell dilution. Control clones were generated from OK cells electroporated with recombinant Cas9 and empty pHRS vector. Knockout clones were identified by Western blotting. Sequences from at least eight bacterial colonies form each clone were used to confirm allele sequences. Two independent clones with distinct mutant alleles were characterized for each KO cell line.

For all experiments, 4×10^5 cells were seeded onto 12-mm Transwell permeable supports (Costar, 3401) in 12-well dishes. After overnight incubation, the filters were transferred to an orbital platform shaker in the incubator and rotated at 146 rpm for 72 h with daily medium changes.

Western blotting

CRISPR/Cas9 control and KO OK cell lines were washed with ice-cold phosphate-buffered saline (PBS). Filters were excised and cells solubilized for 20 min at 4°C on a rotating platform shaker in 0.2 ml detergent buffer (50 mM Tris pH 8.0; 62.5 mM EDTA; 1% IGEPAL, 4 mg/ml deoxycholate) supplemented with 5 μg/ml leupeptin; 7 μg/ml pepstatin A; 1 mM PMSF; and a Pierce Protease Inhibitor Mini Tablet (Thermo Scientific, A32955; 1 tablet/10 ml of buffer). Protein concentration was measured using a D_C Protein Assay Kit (Bio-Rad, 5000111) and equivalent amounts of total protein were separated by SDS–PAGE. Details and sources for the antibodies used in this study are provided in Supplemental Table S1. All blots were imaged using the Bio-Rad ChemiDoc Touch Imaging System and band intensities were quantified using Bio-Rad Image Lab software.

Albumin uptake

OK cells were incubated under continued orbital shear stress for 15 or 30 min at 37°C with the indicated concentration of AlexaFluor-647 albumin (Invitrogen A34785) added apically in serum-free DMEM/F12 supplemented with 25 mM HEPES, pH 7.2–7.5. Filters were washed three times with cold PBS (with Mg^{2+} and Ca^{2+}), cells were solubilized, and cell-associated AlexaFluor-647 fluorescence intensity was quantified by spectrofluorimetry. To visualize cell-associated albumin, filters were incubated with albumin as described above for 15 min, washed twice in warm PBS/+Ca^{2+}/+Mg^{2+} (D8662, Sigma), and fixed for 15 min at ambient temperature in warm 4% paraformaldehyde-100 mM sodium cacodylate. After two washes in PBS, filters were cut from their supports, mounted onto glass slides with ProLong Glass Antifade Mountant (Molecular Probes, P36981), and imaged on a Leica SP8 confocal microscope using a 63× oil immersion objective.

Mathematical deconvolution of albumin uptake curves

OK cells were incubated with the indicated range of albumin concentrations for 15 min and cell-associated albumin quantified by spectrofluorimetry. Albumin uptake curves were deconvoluted using the three-pathway model described previously (Ren *et al*., 2020). This model includes saturable binding components with high (C1, ~50 μg/ml) and low (C2, ~300 μg/ml) affinities and a nonsaturable uptake component (C3). Maximum velocities for each component (V1, V2, V3) were calculated to determine the contribution of each pathway to overall uptake. Uncertainties for the mean value of each parameter $(\partial\bar{x})$ were propagated from the uncertainty of the fitted parameter for each experiment (∂x). For V2/V1, we first propagated the uncertainties ∂V1 and ∂V2 to derive $\partial\frac{V2}{V1}$ in each experiment:

$$\partial\frac{V2}{V1} = \frac{V2}{V1}\sqrt{\left(\frac{\partial V1}{V1}\right)^2 + \left(\frac{\partial V2}{V2}\right)^2}$$

We then propagated uncertainties for each parameter x to the sample mean $(\bar{x})$ according to

$$\partial\bar{x} = \frac{\sqrt{\partial x_1^2 + \partial x_2^2 + \ldots + \partial x_n^2}}{n}$$

Quantitation of dextran-positive and EEA1-positive compartments

Spot counting was carried out with a function written in MATLAB 2019b. Briefly, maximum projections were background-subtracted to remove the lowest 30% of pixel intensity values from the whole image. The image was sharpened and then smoothed by applying a two-dimensional Gaussian filter with a sigma of 0.7. The contrast of the image was increased by local Laplacian filtering with sigma of 100 and alpha of 0.9. Low-intensity peaks were removed and the image was binarized by global thresholding. Regional maxima were detected in the transformed image before binarization. A mask of the binary image was generated using the regional maxima, and masked objects, excluding those in contact with the edge, were counted.

Electron microscopy

OK cells were fixed in 2.5% glutaraldehyde for 1 h, washed with PBS, postfixed for 1 h in 1% osmium tetroxide with 1% potassium

ferricyanide, and washed with PBS. Filters were dehydrated in a graded series of 30–100% alcohol and infiltrated with pure epon three times for 1 h each. Samples were cut and embedded in pure epon for 24 h at 37°C and were cured for 48 h at 60°C. The samples were then sectioned, mounted on grids, stained with 2% uranyl acetate and lead citrate, and examined using a JEM-1400 Plus transmission electron microscope (JEOL).

Immunofluorescence staining of opossum kidney cells

OK cells were washed twice in warm PBS/+Ca^{2+}/+Mg^{2+} and fixed in warm 4% paraformaldehyde/100 mM sodium cacodylate (3 mm $CaCl_2$, 3 mm $MgCl_2$, and 3 mm KCl, pH 7.4) for 15 min at ambient temperature. After two washes in PBS, the filters were quenched (PBS/20 mM glycine/75 mM ammonium chloride) for 5 min and permeabilized for 5 min in quench solution containing 0.1% TritonX-100. After being rinsed with PBS, the filters were blocked with PBS/1% BSA/0.1% saponin for 30 min and incubated for 1 h with primary antibodies (Supplemental Table S1) diluted in wash buffer (PBS/0.5% BSA/0.025% saponin). The filters were washed three times in wash buffer and then incubated for 30 min with secondary antibodies (Supplemental Table S1). Filters were washed in wash buffer three times for 5 min each and then cut and mounted onto glass slides with ProLong Glass Antifade Mountant (Molecular Probes, P36981). Filters were imaged on a Leica Stellaris-8 inverted confocal microscope using a 63× oil immersion objective. Images were acquired and processed using identical conditions, and maximum projections are shown. Images in Figures 6 and 7 were acquired with a voxel size of 45 × 45 × 130 nm (*x*, *y*, *z*). All images were deconvolved with Huygens Essential version 17.04 using the CMLE algorithm, with SNR: 20 and 40 iterations (Scientific Volume Imaging, the Netherlands, http://svi.nl).

Generation of minimegalin-expressing opossum kidney cells

OK cells (4×10^5) added to the apical chamber of 12-mm Transwell supports were immediately transfected using the Invitrogen protocol for lipofectamine 3000 with 1 µg plasmid encoding HA-minimegalin-mCherry, encoding a dually tagged truncated megalin construct originally obtained from the Farquhar laboratory (Takeda *et al.*, 2003; Cui *et al.*, 2010). Transfection medium was removed 6 h later.

Cell surface biotinylation of cubilin

Parental OK cells, control clones, and CRISPR/Cas9 KO clones cultured on 12-mm Transwell supports were apically biotinylated as described in Shipman *et al.* (2023). Cells were solubilized and 10% was reserved to calculate total cubilin. Biotinylated proteins were recovered from the remaining fractions, and the fraction at the cell surface was quantified after SDS–PAGE and western blotting.

Immunofluorescence of mouse kidney cortex sections

All animal protocols conform to the National Institutes of Health *Guide for the Care and Use of Laboratory Animals* and were approved by the University of Pittsburgh Institutional Animal Care and Use Committee. *Lrp2* lox/lox mice (Leheste *et al.*, 1999) were originally provided by Thomas Willnow, Max Delbrück Center for Molecular Medicine, crossed with EMX-Cre mice provided by Cecilia Lo (University of Pittsburgh). These mice have a >95% reduction in kidney megalin expression based on Western blotting (unpublished) and indirect immunofluorescence (Long *et al.*, 2022). Sections (10 µm) of paraformaldehyde-fixed kidneys (from 10 wk–old male mice) cut by the Pitt Biospecimen Core were rehydrated in PBS for 30 min, permeabilized with 0.1% Triton X-100 for 10 min, and blocked with PBS/1% BSA/0.1% saponin/5% normal goat serum for 15 min at room temperature. Double-label staining was performed using the antibodies in Supplemental Table S1 using the methods described in (Shipman *et al.*, 2022). Sections were mounted using Prolong Gold antifade (P10144, Invitrogen) and imaged on a Leica Stellaris-8 inverted confocal microscope using a 63× oil immersion objective.

Electron microscopy of mouse kidney cortex sections

Mouse kidney slices from 16-wk old female littermates were placed in Karnovsky's fixative (2% paraformaldehyde and 2% glutaraldehyde in 0.1 M PBS) and processed for electron microscopy by the Center for Biological Imaging as described in Long *et al.* (2017). Sections were imaged using a JEM-1400 Plus transmission electron microscope.

FUNDING

This research was supported by NIH grants R01 DK118726, F31 DK121394, P30 DK079307, S10 OD021627, S10 OD028596, and P30 CA047904 and by the China Scholarship Council.

ACKNOWLEDGMENTS

We thank Daniel Biemesderfer and Peter Aronson for providing the MC-200 anti-megalin antibody, and Thomas Willnow and Cecilia Lo for sharing the *Lrp2* EMX-Cre mouse strain. We are grateful to the Pittsburgh Center for Kidney Research and Center for Biological Imaging for assistance with fluorescence and electron microscopy (supported by P30 DK079307). This project used the UPMC Hillman Cancer Center and Tissue and Research Pathology/Pitt Biospecimen Core shared resource, which is supported in part by award P30 CA047904.

REFERENCES

Amsellem S, Gburek J, Hamard G, Nielsen R, Willnow TE, Devuyst O, Nexo E, Verroust PJ, Christensen EI, Kozyraki R (2010). Cubilin is essential for albumin reabsorption in the renal proximal tubule. J Am Soc Nephrol 21, 1859–1867.

Beenken A, Cerutti G, Barasch J, Guo Y, Sheng Z, Erdjument-Bromage H, Aziz Z, Robbins-Juarez SY, Chavez EY, Ahlsen G, *et al.* (2023). Structures of LRP2 reveal a molecular machine for endocytosis. Cell 186, 821–836.e13.

Buss F, Arden SD, Lindsay M, Luzio JP, Kendrick-Jones J (2001). Myosin VI isoform localized to clathrin-coated vesicles with a role in clathrin-mediated endocytosis. EMBO J 20, 3676–3684.

Christensen EI, Birn H, Storm T, Weyer K, Nielsen R (2012). Endocytic receptors in the renal proximal tubule. Physiology (Bethesda) 27, 223–236.

Cui S, Guerriero CJ, Szalinski CM, Kinlough CL, Hughey RP, Weisz OA (2010). OCRL1 function in renal epithelial membrane traffic. Am J Physiol Renal Physiol 298, F335–F345.

Dachy A, Paquot F, Debray G, Bovy C, Christensen EI, Collard L, Jouret F (2015). In-depth phenotyping of a Donnai–Barrow patient helps clarify proximal tubule dysfunction. Pediatr Nephrol 30, 1027–1031.

De S, Kuwahara S, Saito A (2014). The endocytic receptor megalin and its associated proteins in proximal tubule epithelial cells. Membranes (Basel) 4, 333–355.

Duan Y, Weinstein AM, Weinbaum S, Wang T (2010). Shear stress-induced changes of membrane transporter localization and expression in mouse proximal tubule cells. Proc Natl Acad Sci USA 107, 21860–21865.

Eshbach ML, Sethi R, Avula R, Lamb J, Hollingshead DJ, Finegold DN, Locker JD, Chandran UR, Weisz OA (2017). The transcriptome of the *Didelphis virginiana* opossum kidney OK proximal tubule cell line. Am J Physiol Renal Physiol 313, F585–F595.

Eshbach ML, Weisz OA (2017). Receptor-mediated endocytosis in the proximal tubule. Annu Rev Physiol 79, 425–448.

Kozyraki R, Fyfe J, Verroust PJ, Jacobsen C, Dautry-Varsat A, Gburek J, Willnow TE, Christensen EI, Moestrup SK (2001). Megalin-dependent cubilin-mediated endocytosis is a major pathway for the apical uptake of transferrin in polarized epithelia. Proc Natl Acad Sci USA 98, 12491–12496.

Kur E, Christa A, Veth KN, Gajera CR, Andrade-Navarro MA, Zhang J, Willer JR, Gregg RG, Abdelilah-Seyfried S, Bachmann S, *et al.* (2011). Loss of Lrp2 in zebrafish disrupts pronephric tubular clearance but not forebrain development. Dev Dyn 240, 1567–1577.

Larsen C, Etzerodt A, Madsen M, Skjødt K, Moestrup SK, Andersen CBF (2018). Structural assembly of the megadalton-sized receptor for intestinal vitamin B12 uptake and kidney protein reabsorption. Nat Commun 9, 5204.

Leheste JR, Rolinski B, Vorum H, Hilpert J, Nykjaer A, Jacobsen C, Aucouturier P, Moskaug JØ, Otto A, Christensen EI, Willnow TE (1999). Megalin knockout mice as an animal model of low molecular weight proteinuria. Am J Pathol 155, 1361–1370.

Limbutara K, Chou C-L, Knepper MA (2020). Quantitative proteomics of all 14 renal tubule segments in rat. J Am Soc Nephrol 31, 1255–1266.

Long KR, Rbaibi Y, Bondi CD, Ford BR, Poholek AC, Boyd-Shiwarski CR, Tan RJ, Locker JD, Weisz OA (2022). Cubilin-, megalin-, and Dab2-dependent transcription revealed by CRISPR/Cas9 knockout in kidney proximal tubule cells. Am J Physiol Renal Physiol 322, F14–F26.

Long KR, Shipman KE, Rbaibi Y, Menshikova EV, Ritov VB, Eshbach ML, Jiang Y, Jackson EK, Baty CJ, Weisz OA (2017). Proximal tubule apical endocytosis is modulated by fluid shear stress via an mTOR-dependent pathway. Mol Biol Cell 28, 2508–2517.

Louvard D (1980). Apical membrane aminopeptidase appears at site of cell-cell contact in cultured kidney epithelial cells. Proc. Natl. Acad. Sci. USA 77, 4132–4136.

Maunsbach AB (1966). Absorption of ferritin by rat kidney proximal tubule cells. J Ultrastruct Res 16, 1–12.

Maurer ME, Cooper JA (2006). The adaptor protein Dab2 sorts LDL receptors into coated pits independently of AP-2 and ARH. J Cell Sci 119, 4235–4246.

Mellor P, Furber LA, Nyarko JNK, Anderson DH (2012). Multiple roles for the p85α isoform in the regulation and function of PI3K signalling and receptor trafficking. Biochem J 441, 23–37.

Morris SM, Arden SD, Roberts RC, Kendrick-Jones J, Cooper JA, Luzio JP, Buss F (2002a). Myosin VI binds to and localises with Dab2, potentially linking receptor-mediated endocytosis and the actin cytoskeleton. Traffic 3, 331–341.

Morris SM, Tallquist MD, Rock CO, Cooper JA (2002b). Dual roles for the Dab2 adaptor protein in embryonic development and kidney transport. EMBO J 21, 1555–1564.

Nagai J, Christensen EI, Morris SM, Willnow TE, Cooper JA, Nielsen R (2005). Mutually dependent localization of megalin and Dab2 in the renal proximal tubule. Am J Physiol Renal Physiol 289, F569–F576.

Oleinikov AV, Zhao J, Makker SP (2000). Cytosolic adaptor protein Dab2 is an intracellular ligand of endocytic receptor gp600/megalin. Biochem J 347(Pt 3), 613–621.

Park HJ, Fan Z, Bai Y, Ren Q, Rbaibi Y, Long KR, Gliozzi ML, Rittenhouse N, Locker JD, Poholek AC, Weisz OA (2020). Transcriptional programs driving shear stress-induced differentiation of kidney proximal tubule cells in culture. Front Physiol 11, 587358.

Pedersen GA, Chakraborty S, Steinhauser AL, Traub LM, Madsen M (2010). AMN directs endocytosis of the intrinsic factor-vitamin B(12) receptor cubam by engaging ARH or Dab2. Traffic 11, 706–720.

Perea-Gomez A, Cases O, Lelièvre V, Pulina MV, Collignon J, Hadjantonakis A-K, Kozyraki R (2019). Loss of Cubilin, the intrinsic factor-vitamin B12 receptor, impairs visceral endoderm endocytosis and endodermal patterning in the mouse. Sci Rep 9, 10168.

Pereira EM, Labilloy A, Eshbach ML, Roy A, Subramanya AR, Monte S, Labilloy G, Weisz OA (2016). Characterization and phosphoproteomic analysis of a human immortalized podocyte model of Fabry disease generated using CRISPR/Cas9 technology. Am J Physiol Renal Physiol 311, F1015–F1024.

Raghavan V, Rbaibi Y, Pastor-Soler NM, Carattino MD, Weisz OA (2014). Shear stress-dependent regulation of apical endocytosis in renal proximal tubule cells mediated by primary cilia. Proc Natl Acad Sci USA 111, 8506–8511.

Ren Q, Gliozzi ML, Rittenhouse NL, Edmunds LR, Rbaibi Y, Locker JD, Poholek AC, Jurczak MJ, Baty CJ, Weisz OA (2019). Shear stress and oxygen availability drive differential changes in opossum kidney proximal tubule cell metabolism and endocytosis. Traffic 20, 448–459.

Ren Q, Weyer K, Rbaibi Y, Long KR, Tan RJ, Nielsen R, Christensen EI, Baty CJ, Kashlan OB, Weisz OA (2020). Distinct functions of megalin and cubilin receptors in recovery of normal and nephrotic levels of filtered albumin. Am J Physiol Renal Physiol 318, F1284–F1294.

Riquier ADM, Lee DH, McDonough AA (2009). Renal NHE3 and NaPi2 partition into distinct membrane domains. J Am Soc Nephrol 296, C900–C910.

Shipman KE, Baty CJ, Long KR, Rbaibi Y, Cowan IA, Gerges M, Marciszyn AL, Kashlan OB, Tan RJ, Edwards A, Weisz OA (2023). Impaired endosome maturation mediates tubular proteinuria in dent disease cell culture and mouse models. J Am Soc Nephrol 34, 619–640.

Shipman KE, Long KR, Cowan IA, Rbaibi Y, Baty CJ, Weisz OA (2022). An adaptable physiological model of endocytic megalin trafficking in opossum kidney cells and mouse kidney proximal tubule. Function (Oxf) 3, zqac046.

Takeda T, Yamazaki H, Farquhar MG (2003). Identification of an apical sorting determinant in the cytoplasmic tail of megalin. Am J Physiol Cell Physiol 284, C1105–C1113.

Wang T, Weinbaum S, Weinstein AM (2017). Regulation of glomerulotubular balance: flow-activated proximal tubule function. Pflugers Arch 469, 643–654.

Yuseff MI, Farfan P, Bu G, Marzolo M-P (2007). A cytoplasmic PPPSP motif determines megalin's phosphorylation and regulates receptor's recycling and surface expression. Traffic 8, 1215–1230.

Zhang F, Zhao Y, Chao Y, Muir K, Han Z (2013). Cubilin and amnionless mediate protein reabsorption in *Drosophila* nephrocytes. J Am Soc Nephrol 24, 209–216.